Design, fabrication, and characterization of a high-field high-temperature superconducting Bi-2212 accelerator dipole magnet

Tengming Shen,[1,*] Laura Garcia Fajardo,[2] Cory Myers,[1] Aurelio Hafalia, Jr.,[2] Jose Luis Rudeiros Fernández,[1] Diego Arbelaez,[2] Lucas Brouwer,[1] Shlomo Caspi,[2] Paolo Ferracin,[1] Stephen Gourlay,[1] Maxim Marchevsky,[1] Ian Pong,[1] Soren Prestemon,[2] Reed Teyber,[1] Marcos Turqueti,[2] Xiaorong Wang,[1] Jianyi Jiang,[3] Ernesto Bosque,[3] Jun Lu,[3] Daniel Davis,[3] Ulf Trociewitz,[3] Eric Hellstrom,[3] and David Larbalestier[3]

[1]*Accelerator Technology and Applied Physics Division, Lawrence Berkeley National Laboratory, Berkeley, California 94720, USA*

[2]*Engineering Division, Lawrence Berkeley National Laboratory, Berkeley, California 94720, USA*

[3]*Applied Superconductivity Center, National High Magnetic Field Laboratory, Tallahassee, Florida 32310, USA*

(Received 15 June 2022; accepted 10 October 2022; published 7 December 2022)

The use of high-field superconducting magnets has furthered the development of medical diagnosis, fusion research, accelerators, and particle physics. High-temperature superconductors enable magnets more powerful than those possible with Nb-Ti (superconducting transition temperature T_c of 9.2 K) and Nb_3Sn (T_c of 18.4 K) conductors due to their very high critical field B_{c2} of greater than 100 T near 4.2 K. However, the development of high-field accelerator magnets using high-temperature superconductors is still at its early stage. We report the construction of the world's first high-temperature superconducting $Bi_2Sr_2CaCu_2O_x$ (Bi-2212 with T_c of ~82 K) accelerator dipole magnet. The magnet is based on a canted-cosine-theta design with Bi-2212 Rutherford cables. A high critical current was achieved by an overpressure processing heat treatment. The magnet was constructed from a nine-strand Rutherford cable made from industrial 0.8 mm wires. At 4.2 K, it reached a quench current of 3600 A and a dipole field of 1.64 T in a bore of 31 mm. The magnet did not exhibit the undesirable quench training common in Nb-Ti and Nb_3Sn accelerator magnets. It quenched a dozen times without degradation. The magnet exhibited low magnetic field hysteresis (<0.1%) as measured by a cryogenic Hall sensor. It was fast cycled to 1.47 T at 0.54 T/s without quenches. This work validates the canted-cosine-theta Bi-2212 dipole magnet design, illustrates the fabrication scheme, and establishes an initial performance benchmark.

DOI: 10.1103/PhysRevAccelBeams.25.122401

I. INTRODUCTION

Nb-Ti superconducting magnets enabled the Tevatron [1], the Heavy Electron Ring Accelerator (HERA) [2], the Relativistic Heavy Ion Collider (RHIC) [3,4], and the Large Hadron Collider (LHC) [5] whereas Nb_3Sn magnets are key to the high-luminosity LHC [6] and the International Thermonuclear Experimental Reactor (ITER). LHC Nb-Ti main dipole magnets were developed to operate at 1.9 K, delivering 8.3 T whereas the high-luminosity LHC interaction region quadrupole magnets have a peak field of ~12 T. Beyond Nb-Ti and Nb_3Sn, several high-temperature cuprate superconductors offer a critical field B_{c2} of greater than 100 T near the liquid helium temperature and have been developed into practical conductors with high critical current density and long length. For particle physics, the potential of high-temperature superconducting magnets was recognized in the 2020 update of the European Strategy for Particle Physics [7]. For a multi-TeV muon collider, 30–50 T high-field solenoids based on high-temperature superconductors are critical for reducing the transverse beam emittance by orders of magnitude [8]. The field limit of high-temperature superconducting magnet technology thus has a strong influence on the design of muon and proton accelerators and the reach of physics. Outside particle physics, such a high-field magnet technology has many applications and may even be revolutionary. For example, high-field superconducting magnets working at a peak field of 20 T at 20 K based on high-temperature superconductors are the key to the commercial fusion community's pursuit of compact, Tokamak-type fusion reactors [9].

*Corresponding author.
tshen@lbl.gov

The development of high-field superconducting magnets using high-temperature superconducting materials has led to several successes, mostly in solenoids. An all-superconducting 32 T, 30 mm bore solenoid was constructed at the National High Magnetic Field Lab (NHMFL) from REBCO-coated conductors, with 17 T REBCO coils nested concentrically inside Nb-Ti and Nb_3Sn coils [10,11]. Bruker Corporation has delivered stable, homogeneous magnets (28 T, 80 mm bore) for solid-state protein 1.2 GHz nuclear magnetic resonance (NMR) applications in structural biology, which is also based on the REBCO-coated conductor [12].

However, the development of accelerator magnets using high-temperature superconductors is at an early stage. A primary reason is that, like Nb_3Sn, they are brittle and the critical current is sensitive to strain. The critical current would be irreversibly degraded due to excessive strain from winding, thermal and electromagnetic cycles, and quenches, during which a portion of the coil loses superconductivity and heats up. Handling such conductors requires a sensible magnet design and robust fabrication process. Additionally, the superconducting accelerator magnets need a multi-kA cable. For round strands like Nb-Ti and Nb_3Sn, an effective solution is high-current Rutherford cables, a flat rectangular or slightly keystoned cable that is simple and relatively inexpensive to produce. In a circular collider, magnets need to provide a high-quality magnetic field seen by particles over the full dynamic range from field injection through collision [4,13]. The field errors need to be of the order of 10^{-4} of the central bending field for stable beam behavior, and thus, of the order of a few 0.1 mT. Rutherford cables are composed of wires twisted and transposed for stability and high field quality required for accelerating particle beams and achieving high beam quality. REBCO-coated conductor is only available in a thin tape and the critical current is anisotropic in the magnetic field. This requires that new solutions must be explored to turn it into a practical cable. CERN has proposed an aligned block dipole magnet design [14,15] based on a ROEBEL cable [16], a flat cable assembled from meandered punched REBCO tapes. The design is effective in maximizing the use of the critical current density (J_c) as the magnetic field is mostly parallel to the tape surface, the orientation where the critical current is at a maximum. A drawback is that the ROEBEL cable requires cutting away ∼40% of coated conductor, rendering a higher cost and potentially increasing the vulnerability of the cable mechanically against thermal and powering cycles. Lawrence Berkeley National Lab (LBNL) has constructed dipole magnets using a CORC® (conductor on round core) cable, made with REBCO tapes wound spirally on a round Cu core, based on a canted-cosine-theta design [17–20] that will be further discussed in Sec. II. For any CORC® magnet, a challenge is meeting field quality requirements needed by accelerator magnets due to the large magnetization of REBCO tapes. The magnetization of superconductors is proportional to $J_c \times d_{\text{eff}}$, where d_{eff} is large for REBCO tapes since they are available as a single filament conductor. d_{eff} is large for REBCO tapes when the magnetic field is not parallel to the tape.

Another technical path uses Bi-2212, a multifilamentary round wire like Nb-Ti and Nb_3Sn [21]. Recently, it has been shown to carry a high critical current density (J_E of 1000 A/mm^2 at 4.2 K and 27 T) and km lengths of conductors by the U.S. Magnet Development Program and industry collaborators [22,23]. Being a round wire, it can be made into a Rutherford cable. Leveraging such progress, Bi-2212 Rutherford cables have been fabricated into flat racetrack coils, which achieved a wire J_E of 1000 A/mm^2 at 4.2 K and 3.6 T using an overpressure processing heat treatment [23,24]. Racetrack coils are fundamental building blocks for a block-type magnet design, which has been the design of choice for LBNL's HD2 Nb_3Sn dipole magnet (13.8 T, 36 mm clear aperture) [25] and CERN's Nb_3Sn racetrack test magnet (16.2 T, no clear aperture) [26]. However, Bi-2212 Rutherford cables have exhibited 5% critical current degradation under a transverse pressure of ∼120 MPa [27] and will likely not be sufficiently strong to bear high stress in a block-type, 20 T accelerator magnet. Another possible design is a conventional cosine-theta magnet that also has the problem of high transverse pressure on the superconductor cables. Another complexity is that the overpressure processing heat treatment reduces the wire diameter by ∼3–4% [21,28]. In the case of block-type magnets and cosine-theta windings, the shrinkage would accumulate across the entire winding, making it difficult to optimize the coil geometry; this is the inverse of what occurs in Nb_3Sn windings for which the wire or cable swells by ∼2–4%. In addressing stress management, Fermilab is exploring a stress-managed cosine-theta magnet design [29] and moving toward building prototype magnets with both Nb_3Sn and Bi-2212 coils.

II. MAGNET DESIGN

For this work, we selected a canted-cosine-theta magnet design [30]. Figure 1 provides a schematic view of the design concept. The central components are mandrels made from cylindrical metal tubes with machined grooves, which contain the individual turns of superconducting cables. The grooves define the shape of the winding and accept the cable dimensional change locally without accumulation. A drawback of the canted-cosine-theta design is that, as compared to a perfect cosine-theta winding, the field generation efficiency is reduced by the introduction of the interturn rib, which dilutes the winding current density by ∼15–20%, and then further by the tilted winding, which introduces a small solenoidal field and reduces field efficiency by another ∼5%. The most important strength of the design is that a canted-cosine-theta magnet comes

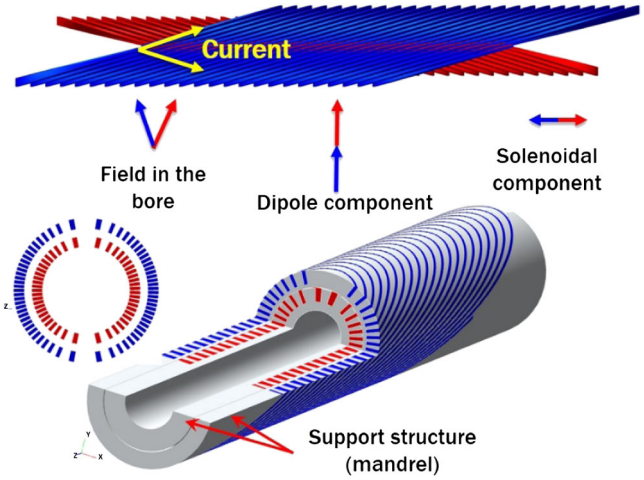

FIG. 1. Schematics of a canted-cosine-theta dipole magnet. The superconductor windings (the layer 1 coil in red and the layer 2 coil in blue) sit inside grooves in metal mandrels (in gray) and are shaped by, and mechanically protected by, the mandrels during fabrication and electromagnetic cycles. A cross-sectional cut reveals a cosine-theta-like current distribution that delivers the good field quality required by a high-energy physics collider accelerator magnet. Reproduced with permission from [31].

with stress management ability; the Lorentz force on the superconducting cable is intercepted locally by the ribs that separate the turns. The ribs between turns transfer magnetic forces to the mandrel by a cantilever effect. This ability is important for high-field magnets because magnetic forces increase with field strength as B^2, and a canted-cosine-theta coil should be less likely to suffer appreciably from reversible I_c reduction or irreversible superconductor degradation due to precompression of the coil and magnetic forces. Another benefit is that the canted-cosine-theta coil requires a minimal set of tooling. The conventional

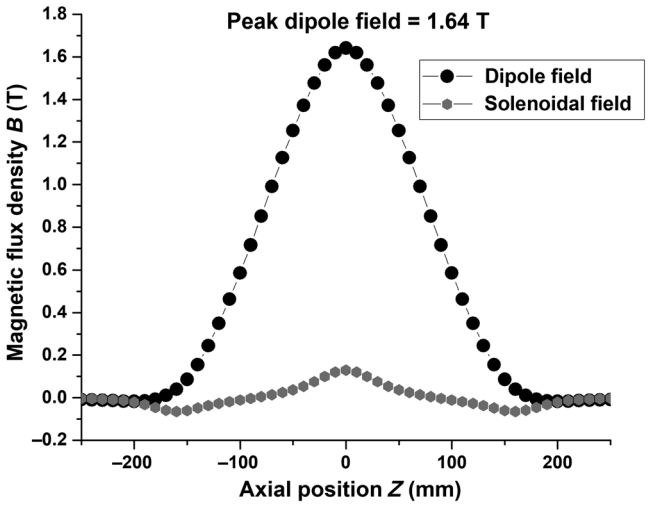

FIG. 2. Magnet field distribution along the central axis of the magnet at an operation current of 3.6 kA.

TABLE I. Specification of the two layers of coils.

	Layer 1	Layer 2
Mandrel OD (mm)	47.3	64.7
Mandrel ID (mm)	30.8	51.3
Mandrel length (cm)	39	39
Number of turns	16	16
Winding tilt angle (degree)	15	15
Cable length per coil (m)	5.7	8
Peak field at the conductor (T)@3600 A	1.92 T	1.58 T
Dipole field in the bore (T)	1.64 T@3600 A	
Operating temperature (K)	4.2	

OD = outer diameter; ID = inner diameter.

cosine-theta design for Nb_3Sn and Bi-2212 requires dedicated, multiple sets of tooling to handle winding, reaction, epoxy impregnation, and structural loading. Figure 2 and Table I present the parameters of the coils that were constructed.

III. MAGNET CONSTRUCTION AND TEST

A. Conductor design and performance

Table II lists the specifications of the strand and cable. The cable was made from a strand of 0.8 mm (55×18 design of 18 bundles each containing 55 filaments, untwisted, strand ID PMM170725) fabricated by Bruker OST LLC using the powder-in-tube method. The strand was fabricated with a precursor powder (batch LXB86) fabricated by Engi-Mat LLC with a nanospray combustion method [22,23]. The wire has 990 filaments embedded in

TABLE II. Specification of the superconductor strand and the cable.

Strand design	55×18
Strand diameter (before reaction) (mm)	0.8
Strand diameter (after reaction) (mm)	~0.78
Powder composition	$Bi_{2.17}Sr_{1.94}Ca_{0.89}Cu_2O_x$–called 521
Average filament diameter (μm) when densified	~11
Cable design	Nine-strand Rutherford cable
Cable nominal dimensions (before reaction)	4.0×1.44 mm^2
Cable nominal dimensions (after reaction)	$\sim 3.9 \times 1.4$ mm^2
Cable transposition pitch (mm)	25.5
Wire twist pitch (mm)	26.3

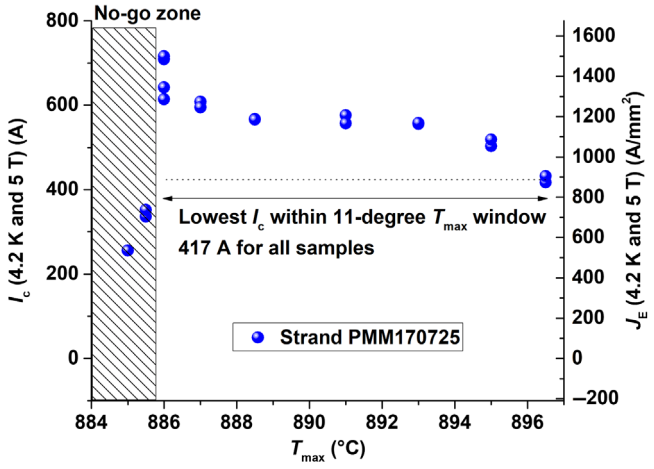

FIG. 3. The strand critical current I_c and engineering critical current density J_E at 4.2 K and 5 Tesla (perpendicular to wire) as a function of the maximum heat treatment temperature T_{max}. The sample is 5–10 cm long and reacted in a temperature zone with a temperature gradient no larger than 0.5 °C.

pure Ag matrix, which is again encased in an external sheath of high-strength oxide-dispersion strengthened Ag-0.2wt%Mg. The as-drawn wire has a volumetric Ag:AgMg:Bi-2212 ratio of 0.5:0.25:0.25. Note that during cabling, there was no planetary action and thus the wire was twisted 360° per cable pitch.

The cable was insulated with a thin TiO_2-polymer coating [32–34] and then further insulated with a mullite sleeve (wall thickness ~0.15 mm). Electrical shorts were found in solenoids wound with strands insulated only with thin TiO_2 coating because silver grows through cracks in the TiO_2 coating and shorts the coil [35]. Coils insulated with mullite only have been shown to exhibit leakage, which refers to Bi-2212 liquid leaking from the strands and reacting with surrounding insulation during heat treatment [33]. A combination of a TiO_2 coating with a mullite sleeve was selected because together they effectively prevent electrical shorts between turns and reduce ceramic leakage.

Figure 3 shows the dependence of $I_c(4.2\ \mathrm{K}, 5\ \mathrm{T})$ with the maximum processing temperature T_{max}. The heat treatment is an overpressure melt processing at 50 bar with the oxygen partial pressure at 1 bar. Figure 3 illustrates that the heat treatment consists of two zones, a no-go zone where the temperature is insufficient to melt Bi-2212 filaments and should be avoided and a reaction zone above the melting temperature of 885 °C. Inside the reaction zone, there is a further dependence of I_c on T_{max}. The highest I_c within this window is deemed to be impossible to achieve reliably in coils due to the difficulty of controlling the absolute temperature within a coil with a large thermal mass as precise as ±1 °C. The figure of merit we used to measure and predict magnet performance is the lowest sample I_c obtained from this short sample heat treatment within a 10 °C window; this will be further discussed in Sec. IV. More information about heat treatment control can be found in [36,37].

B. Coil fabrication

The mandrel is a central component of a canted-cosine-theta coil since it behaves both as the winding former and provides structural support. The mandrels are made of 954 aluminum bronze and machined with a four-axis CNC machine (vertical, transverse, axial cutter motion, and mandrel rotation). An additional gap is provided at the pole region to facilitate bending with a small radius of curvature during winding. The mandrel receives a preoxidation heat treatment to develop a thin passivation oxide layer on its surface. Compared to the cosine-theta Nb_3Sn coil fabrication, the process of winding canted-cosine-theta coils is simpler and uses less tooling. For example, to fabricate a cosine-theta Nb_3Sn coil, a process is used to paint the coil with a CTD-1202X binder and cure the coil under pressure at 150 °C making it a solid object for handling [38], whereas the two canted-cosine-theta coils were wound separately on two mandrels and the coils are naturally contained and shaped by their mandrels. During winding, fibers of the mullite sleeve can be damaged, resulting in electric shorts between a coil and its metal mandrel. A key technique we use is painting with a TiO_2 slurry on top of the mullite sleeve of Rutherford cables to repair any potential fiber damages. The coils went through a 50 bar overpressure processing heat treatment in a mixed gas of Ar/O_2 (2 vol.% oxygen) at the National High Magnetic Field Laboratory (NHMFL) with a peak temperature control of ±3 °C. The coils exhibited no electric shorts to the mandrels after winding, after reaction, and during and after tests.

C. Magnet assembly

Reacted coils were instrumented with flexible printed circuit board voltage tap traces and impregnated with a vacuum bag vacuum pressure impregnation approach using an NHMFL mix-61 epoxy resin [39]. The vacuum bag method requires a minimal set of tooling. The impregnated coils were aligned and assembled concentrically with small gaps in between. The gaps are inserted with Kapton bags with multiple pieces of S-2 glass cloths inside. The Kapton bags are then filled with an epoxy resin (CTD-528) at room temperature which then cures at 50 °C for 24 h. The shims prevent relative movement between coils. The vacuum bag impregnation method and the Kapton epoxy resin bag assembly method were also used for Nb_3Sn canted-cosine-theta coils and further described in [40,41]. The two assembled coils were wrapped with Kapton and G-10 and then clamped inside two halves of an aluminum alloy shell held together by aluminum bolts. Figure 4 provides a cross-sectional view

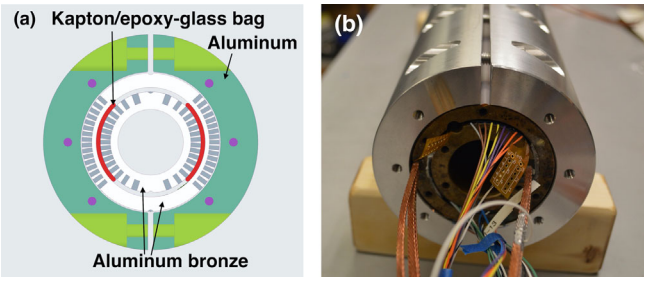

FIG. 4. (a) Cross-sectional view of the assembled magnet. The red arc between two layers of coils is shims made of Kapton/epoxy-glass bags. (b) The as-assembled magnet.

and a photo of the assembled magnet. A small amount of prestress (from −18 to −30 MPa for the outer layer coil and from −2 to 8.75 MPa for the inner layer coil) is expected with cooling to 4.2 K due to the difference between the thermal contraction of aluminum and the coil pack. The strains in the coils are small and were not monitored.

D. Magnet test

The magnet was tested both at 77 and 4.2 K. The 77 K tests provide a quick quality assurance check of coil performance. At 4.2 K, the magnet was driven to quench to determine performance limits. Quench detection was achieved by measuring the terminal voltages of individual coils, their differential, and the entire magnet. The magnet is deemed to quench if the absolute values of any of these voltages exceed 100 mV for longer than 10 ms. Quench protection was achieved with energy extraction into a dump resistor of 20 mΩ. The magnet has a self-inductance of 100 μH. The main dipole field was measured with a cryogenic Hall sensor (HGCT-3020) from Lake Shore Cryotronics and a Keithley 2182 nanovoltmeter operating at ten samples per second.

IV. TEST RESULTS

A. Quench performance

At 4.2 K, the magnet was driven to quench a total of 12 times. Figure 5 shows that it reached a quench current of 3.6 kA and a bore dipole field of 1.64 T. The field constant is 0.4556 T/kA. The peak field on the conductor was 1.92 T. The magnet experienced no quench training, unlike what is typically observed in Nb-Ti and Nb_3Sn magnets. Training refers to the increased quench current with an increasing number of quenches. For canted-cosine-theta magnets, the conductor has an increased interface with mandrels compared to conventional cosine-theta magnets, which may increase the number of quenches to fully train the Nb_3Sn canted-cosine-theta magnet [40]. The quench current slightly increases from 3600 to 3618 A while increasing the current ramp rate from 10 to 100 A/s and then drops to 3606 A at a ramp rate of 200 A/s. The 77 K tests before and after the 4.2 K test indicate that there is no degradation due to quenches or thermal cycles. All quenches occurred in the inner layer coil consistently at the same location (the second turn from one end; it is near the peak field region). Coil resistive voltages were measured using high-precision voltage measurements. When magnet current was held at 2500, 3000, and 3500 A, the inner layer coil showed a resistive voltage of ∼100, ∼250, and ∼790 μV whereas the quench turn exhibited a resistive voltage of ∼3.6, ∼13.4, and ∼87 μV.

B. Fast cycling capability

The magnet was cycled from 0 to 3200 A (1.47 T) at 1000 A/s (Fig. 6). The fast ramping of superconducting accelerator magnets based on Rutherford cables typically

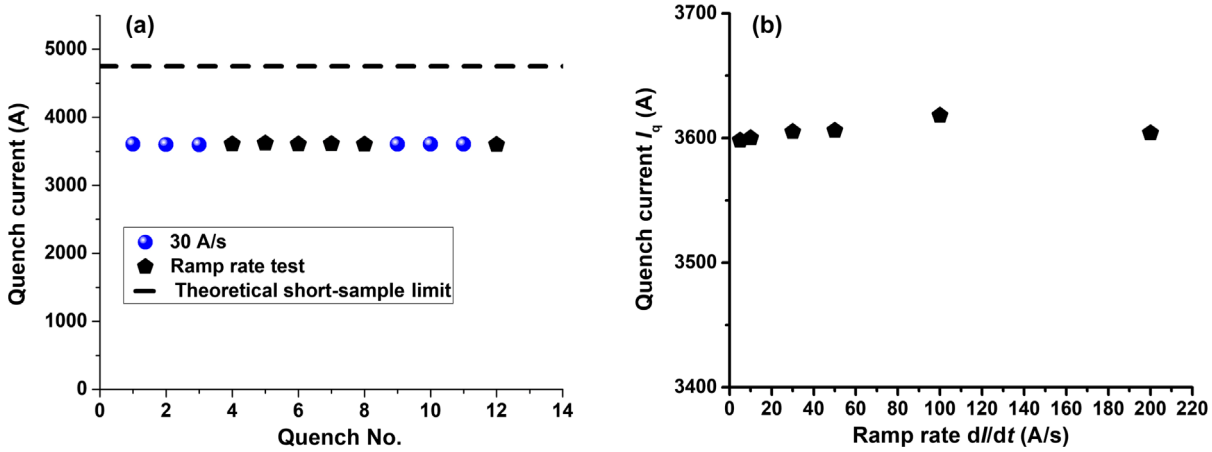

FIG. 5. (a) The quench history of the magnet at 4.2 K with its theoretical short-sample limit; (b) The ramp rate dependence of the magnet quench current at 4.2 K.

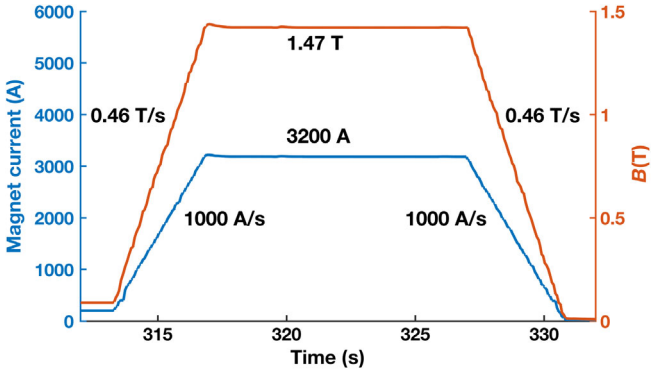

FIG. 6. A fast cycling run of the magnet at 1000 A/s and 0.46 T/s.

results in eddy currents between strands within a cable and coupling currents between filaments within a strand. Such eddy currents lead to a temperature rise and subsequent magnet quench for Nb-Ti and Nb_3Sn magnets due to their low enthalpy margins. Like Nb-Ti, Nb_3Sn, and Bi-2212 behave like a nonlinear magnetic material with magnetization that resists magnetic field change. Such magnetic hysteresis loss contributes to the heating of superconductors. The fast ramping of superconducting accelerator magnets also results in less time for superconductor winding to pass heat to coolant (helium).

C. Field distortion

Figure 7 shows the measured values of the magnet transfer function (TF $= B_1/I$, where B_1 is the main dipole field) measured by the Hall sensor at the center of the magnet during a linear ramp-up, a 10-s hold at the peak current, and a linear ramp down. Without magnetization effects of the aluminum bronze or nonlinear error of the Hall sensor sensitivity, TF should be constant with magnet current. TF decreases with increasing magnet current mostly due to the saturation of magnetization of the aluminum bronze. Also at zero current, there is about ~0.5 mT field due to the remanent magnetization of superconductors. The magnetization of superconductors contributes to errors in the magnetic field. Such magnetization is due to the persistent currents inside the superconductor filaments which shield the filament interiors from the external fields. Thus, the magnetic field is larger with decreasing current than with the increasing current. Such field hysteresis is a good indicator of the magnitude of superconductor magnetization. The valuable info from Fig. 7 is the gap in the transfer function between increasing magnet current and decreasing magnet current and its ratio against the main field.

Figure 8 provides a further measurement of persistent current effects. It shows the main dipole field difference between current increasing and current decreasing measured by the Hall sensor during a staircase current ramp with 120 s at each current plateau. Presumably, the eddy current effects are mostly eliminated at the current holds, and thus the field difference is mostly indicative of the persistent current effect. Note that the field difference trends toward zero when the magnet current is zero because the coil had been magnetized. The persistent current-induced field distortion is found to be small. At 2 kA, the relative contribution of field distortion due to the persistent currents to the main dipole field is about 0.05% (5 units, a unit is 10^{-4} of the main field). Figure 8 indicates that the maximum field distortion occurs between 1000 A (the maximum field on the conductor $B_m = 0.53$ T) and 2000 A ($B_m = 1.06$ T). This indicates that the penetration field of Bi-2212 Rutherford cables, the highest field which can be shielded from the interior of the filament, is between 0.53 and 1.06 T. This is consistent with the Bean model of superconductor magnetization, which predicts $B_p = \mu_0 J_c d_{\text{eff}}/\pi$ at 0.512 T (assuming $J_c = 8000$ A/mm^2 and d_{eff} of 160 μm [42]). Note that Rochester *et al.* [43] measures magnetization of Bi-2212 Rutherford cables and estimated B_p as ~0.4 T.

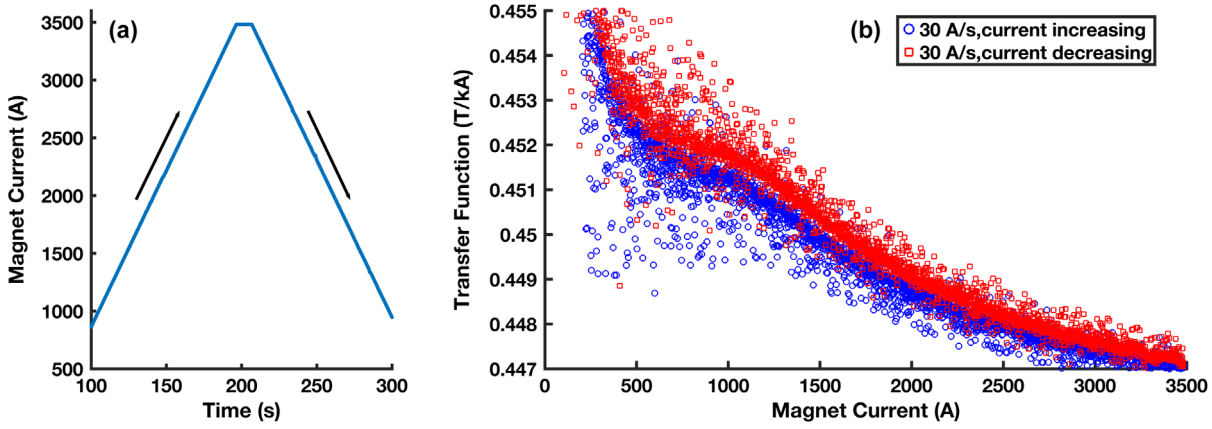

FIG. 7. (a) Magnet current ramps up and down at 30 A/s. (b) Main field transfer function measured. Field was obtained by converting the output voltage of the Hall sensor (In-As) using a mean loaded sensitivity 7.98 mV/T.

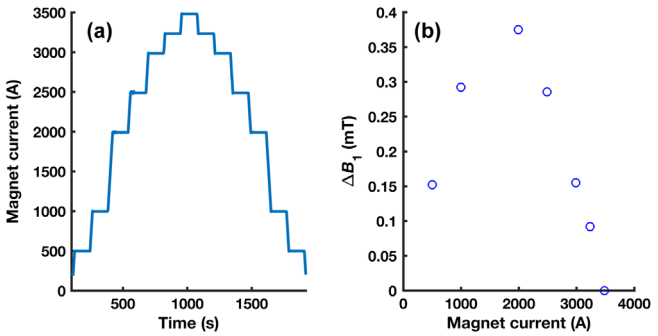

FIG. 8. (a) A staircase magnet current ramp to 3500 A with 120 s holds (current holds at 500, 1000, 2000, 2500, 3000, 3250, 3500 A.). (b) The main dipole field distortion due to persistent current effects of Bi-2212 superconductors, deduced from the field difference between current increasing and current decreasing, during the staircase current ramp. Note that ΔB_1 here is essentially proportional to the width of the magnetization curve of the superconductor after the initial magnetization during which superconducting filaments are penetrated by magnetic flux.

V. DISCUSSION

We described a method of constructing superconducting accelerator magnets from high-temperature superconducting Bi-2212 wires and cables and the performance of a demonstration magnet. In this section, we will examine the field quality and the performance compared to the strand $I_c(B)$ and discuss factors that limit coil performance. We will also discuss the potential uses of this technology and provide an outlook for future work.

A. Performance gap and methods to reduce it

Figure 9 shows the magnet performance versus a "short-sample-limit" $I_{\mathrm{SSL}}(4757\ \mathrm{A})$, which is defined by crossing the magnet load line with the cable $I_c(B)$. The I_{SSL} is commonly used for Nb-Ti and Nb_3Sn magnet design and provides a quantitative measure of magnet performance. Note that the cable critical current is derived from the lowest strand current in the reaction window in Fig. 3. At 3600 A, the central dipole magnetic field in the bore is 1.64 T, and the maximum field on the conductor is 1.92 T. Thus, the magnet quench current is ~76% of I_{SSL}. Clearly, a gap exists between the magnet performance and the I_{SSL} derived from a single wire.

Then this invites the question of whether such a gap is particular to this magnet, and if not, how does it compare to other coils? Figure 10 compares the performance of this magnet to those of other Bi-2212 coils recently tested (BIN5aOL, a single canted-cosine-theta coil, was described in [44] and the performance of RC6, a single racetrack coil, was described in [23]). All of the coils exhibit a performance benchmark that is rather consistent between them, irrespective of coil types and the fact that they were made from cables and precursor powders of different origins, except the high performance of the outlier RC6, which is

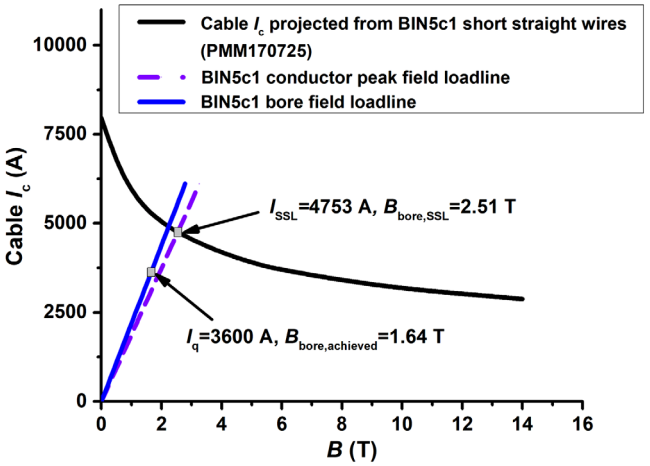

FIG. 9. Magnet loadline versus the cable critical current. The cable critical current was derived from the lowest round strand current in the reaction window in Fig. 3.

rather attributed to the outstanding performance of the strand used in that coil. Again, the $J_E(B)$ presented is derived from the lowest strand current in the reaction window in Fig. 3.

It is thus important to understand what causes such a gap. Our hypothesis is that the performance gap is likely caused by two reasons. The first cause is leakage [28]. In principle, overpressure heat treatment prevents leakage of Bi-2212 from filaments that are driven by the creep rupture of the silver sheath under the buildup of internal pressure, especially nitrogen on heating from ambient to 890 °C. Indeed leakages of individual overpressure processed strands are rare [28]. However, in our coils, we speculate

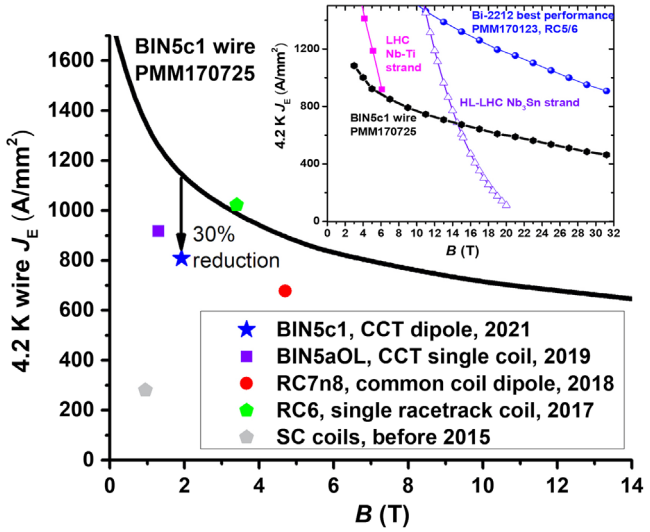

FIG. 10. The performance of the magnet as compared to several other coils tested and the short sample performance. The inset shows $J_E(B)$ of the BIN5c1 wire against that of the record performance of Bi-2212 wires and those of the LHC Nb-Ti main ring dipole strand and HL-LHC Nb_3Sn strand.

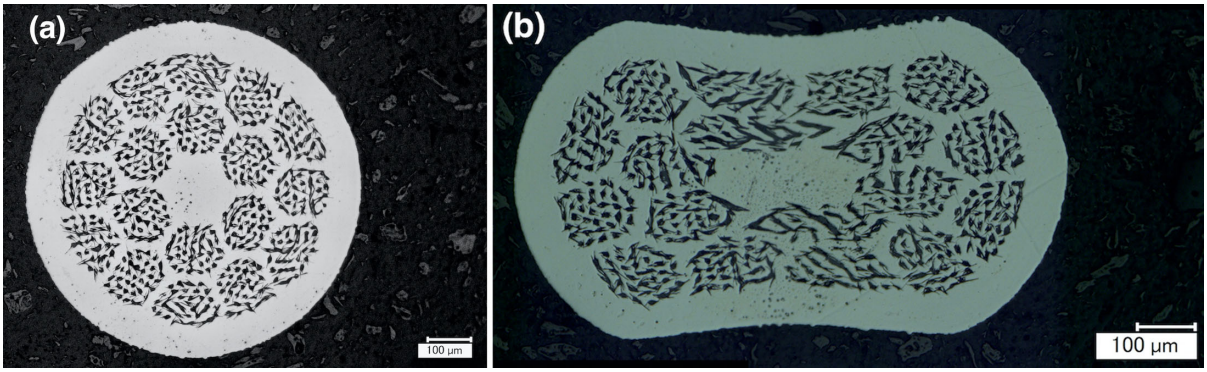

FIG. 11. The strand on the left is a round, 37 × 18, 0.8 mm Bi-2212 wire after a 50 bar overpressure processing heat treatment, after which it is still a round wire despite that its diameter d is reduced to ∼0.78 mm. The strand on the right is the same wire rolled to a thickness t of 0.580 mm and reacted with a 50 bar overpressure processing heat treatment, after which the strand has a peanut shape with its width at 0.957 mm and its thickness varying from 0.502 to 0.550 mm. The four bundles of the rolled strand near the vertical central line are more deformed than others and show a larger degree of filament bonding and bridging. The 4.2 K, self-field I_c of the rolled strand (rolled strain: $(d-t)/d = 0.275$) is ∼13% lower than that of the round strand.

that a chemical reaction between Bi-2212 wires and mullite insulation might be the culprit of additional leakage. The use of TiO_2 as insulation with mullite braid around the TiO_2 interposes an inert barrier to Bi-2212 migration toward the mullite or to the reaction of the mullite with the Ag [45,46]. This combination is almost 100% protective for single-strand wires. Earlier in racetrack coils, we reported that TiO_2 coating on cables could nearly eliminate leakage [24]. The present coils exhibited leakage, despite having a TiO_2 coating, perhaps because the TiO_2 coating used in this work was painted on with a single ceramic base coat. We have noticed that this coating can scrape off during cable spooling and respooling. In the single-strand solenoids made at the NHMFL, an additional 1-2 μm of polymer top coat is added to the TiO_2 layer that significantly increases its abrasion resistance [33] but this is not possible at present for the cable, for which we need to develop a new processing line to provide controlled drying of about 5 min at 200 °C for the top coat. The Bi-2212 leakage also reduces the n-value due to the fluctuations of local I_c that the leakage introduces.

A second possible cause is associated with wire shrinkage during overpressure processing. Figure 11 shows cross sections of a round strand and a rolled strand after overpressure processing heat treatment. The round strand exhibits isotropic shrinkage and we, therefore, expect that the filament spacing has been reduced nearly uniformly. The rolled strand on the right simulates strands in Rutherford cable during the overpressure processing heat treatment. For the rolled strand, wire shrinkage is not uniform, altering filament spacing the most in the middle section and causing filament distortion equivalent to filament sausaging. Filament spacing can have an influence on the filament-to-filament bridging [47] and grain structures. Microscopic observation of the cross section of the BIN5aOL coil and the RC1 coil [24] confirms this observation. This deformation is not expected to alter the high residual resistivity ratio and electrical conductivity of the silver matrix [48]. However, in the case of the rolled strand shown in Fig. 11, the I_c (4.2 K, self-field) decrease was ∼13%. A potential method to alleviate the issue is to preshrink the wire diameter before overpressure processing so that the heat treatment does not cause further nonuniform wire shrinkage in addition to that caused by the cabling process. A proof-of-principle of winding predensified Bi-2212 wires into a coil was provided by Matras *et al.* [49].

B. Explaining quench behaviors

Compared to low-temperature superconducting accelerator magnets, a potential strength of high-temperature superconducting accelerator magnets is the lack of quench training. None of the high-temperature superconducting accelerator magnets built thus far have shown quench training. This work demonstrates that this is also the case for Bi-2212 canted-cosine-theta magnet design at 4.2 K and <2 T, despite having an increased interface between conductor and mandrel. Admittedly, all high-temperature superconducting accelerator magnets built thus far are low field (<5 T). Also, based on Fig. 10, the magnet quenched at the level of ∼76% of its short-sample-limit. Experience with traditional Nb-Ti and Nb_3Sn magnets shows that these magnets also show very small or no training if it only achieved ∼76% of its short-sample limit.

The quench behavior shown in Fig. 5 is not what is typically found with Nb-Ti and Nb_3Sn accelerator magnets and deserves an analysis. Occasionally, some Nb_3Sn magnets demonstrated a reversed ramp rate dependence similar to that shown in Fig. 5(b). We will attempt a semiquantitative analysis to shed light on the physics of heat dissipation of superconductors, what causes quenches

in our magnets, and their similarities and differences with Nb-Ti and Nb_3Sn magnets.

During current ramps, superconducting magnets are warmed up by magnetic hysteresis loss of superconducting filaments and eddy currents between filaments inside a strand and between strands inside a cable. The eddy current loss is characterized by a time constant that is related to the twist pitch length of the strand l_{twist} and the effective transverse resistivity ρ_t of the metal-superconductor composite [2]:

$$\tau = \frac{\mu_0}{2\rho_t}\left(\frac{l_{\text{twist}}}{2\pi}\right)^2 \tag{1}$$

Strands used in this work were untwisted before cabling and twisted 360° per cable pitch during cabling with a l_{twist} of ~26.3 mm. Assuming an equivalent transverse resistivity ρ_t of $7.5 \times 10^{-11}\ \Omega \cdot \text{m}$ between filaments (pure Ag with a residual-resistance-ratio of 210) and ρ_t of $3.5 \times 10^{-9}\ \Omega \cdot \text{m}$ between strands (Ag-0.2 wt.%Mg) [48], τ is 0.14 s for intrastrand eddy currents and 3.2 ms for interstrand eddy currents.

The eddy current-induced heat dissipation per ramp cycle per unit volume is [2]:

$$Q_{\text{CL}} = \frac{B_m^2}{\mu_0}\frac{4\tau}{t_{\text{ramp}}}, \tag{2}$$

where B_m is the peak magnetic field and t_{ramp} is the amount of current ramp time. Thus, compared to intrastrand eddy current loss, the interstrand eddy current loss is rather small. For a current ramp to 3600 A ($B_m \sim 1.92$T), the intrastrand eddy current loss is estimated to be ~14.5 kJ/m^3 for a 30 A/s ramp. It goes up linearly with the ramp rate and is ~97 kJ/m^3 for a 200 A/s ramp. Note that this value is for the entire superconductor strand that includes the stabilizer. This analysis is applicable to Nb-Ti and Nb_3Sn conductors and from it, one can easily understand why the quench current of Nb-Ti and Nb_3Sn magnets usually decreases with increasing current ramp rate.

What then causes the weak ramp rate dependence of the quench current in Fig. 5 and some of Nb_3Sn magnets? Let us perform an analysis, with the assumption that the cause of the reversed ramp rate dependence is that the quenches were caused by index loss-induced joule heating of the superconductors. The first evidence is that incremental resistive voltages were observed at the terminals of our magnet and the quench turn before the quench. When magnet current was held at 2500, 3000, and 3500 A, the quench turn exhibited a resistive voltage of ~3.6, ~13.4, and ~87 μV.

The E-J characteristics of superconductors are described by a power-law relationship:

$$E = E_c\left(\frac{J}{J_c}\right)^n. \tag{3}$$

where E_c is the electrical field criterion (1 μV/cm) and n is the n-value. The joule heating per superconductor volume during current ramping up is described by

$$Q_{\text{IL}} = \int_0^{t_q} EJ\,dt = \int_0^{t_q} E_c\frac{J^{n+1}}{{J_c}^n}dt \tag{4}$$

where J_q is equal to the quench current I_q divided by the superconductor area A_{sc}, Q_{IL} the total power dissipation per volume due to index losses generated during the current ramp. t_q is the time at which quench occurs and is equal to t_{ramp}. Assuming that the current is linearly ramped at a constant rate $dI/dt = k$, then

$$\begin{aligned} Q_{\text{IL}} &= \int_0^{t_q} E_c\frac{J^{n+1}}{{J_c}^n}dt = \int_0^{t_q} E_c\frac{\left(k\cdot\frac{t}{A_{sc}}\right)^{n+1}}{{J_c}^n}dt \\ &= \frac{E_c}{{J_c}^n}\left(\frac{k}{A_{sc}}\right)^{n+1}\frac{(t_q)^{n+2}}{n+2} \\ &= E_c\left(\frac{J_q}{J_c}\right)^n\frac{J_q}{(n+2)}t_q = E_qJ_q\frac{t_q}{(n+2)} \end{aligned} \tag{5}$$

Qualitatively, one can see that Q_{IL} decreases with increasing k. At the quench current of 3600 A, J_q is ~4040 A/mm^2. When the magnet current was held at 3500 A, the averaged electrical field E_q of the quench turn was experimentally determined to be ~2.3 μV/cm. Here to perform a quantitative analysis, one has to guess the n value. Assuming $n = 15$, one arrives at Q_{IL} of >6560 kJ/m^3 for 30 A/s and >984 kJ/m^3 for 200 A/s. Note that this value is for the superconductor filaments only. The average joule heating over the entire superconductor strand that includes the stabilizer is >1312 kJ/m^3 for $k = 30$ A/s. Q_{IL} is reduced to >197 kJ/m^3 for 200 A/s. For the 12 quenches irrespective of the current ramp rate, our experiment demonstrated that the peak dissipated power per unit volume, E_qJ_q, was nearly constant.

The hysteresis loss $Q_{\text{HL}}(\pm 3\ \text{T})$ of a comparable Bi-2212 wire has been measured to be 3000 kJ/m^3 over the Bi-2212 volume [42]. In our case, the field was ramped up to 1.92 T and thus the total hysteresis loss is estimated to be <750 kJ/m^3 over the superconductor volume and <150 kJ/m^3 over the entire wire. Note that both the hysteresis loss and the eddy current loss spread over the entire ramp. At a low ramp rate, the hysteresis loss of the superconductor could be absorbed by the entire coil and the insulation and structural material around it (mandrel in this case). It becomes increasingly difficult for coil winding to pass heat due to hysteresis loss to helium when ramping rate increases. This contributes to why the quench current of Nb-Ti and Nb_3Sn magnets usually decreases with an increasing current ramp rate.

Also, note that the joule heating due to index losses of superconductors concentrates around the quench current. Thus the hysteresis loss plays a less role for our magnet in causing quenches than the joule heating due to index losses of superconductors.

A typical temperature margin for Nb-Ti and Nb_3Sn magnets is ∼1 K above the working temperature, which translates to an enthalpy margin of ∼1.5 kJ/m^3 at 4.2 K, appropriately 10 μJ energy deposited to a 1-cm long section of a Cu wire of 1.0 mm in diameter. The dominant quench mechanisms associated with training for nondegraded Nb-Ti and Nb_3Sn accelerator magnets are, therefore, random, transient point disturbances associated with epoxy cracking or conductor motion or stick-slip motions between conductors and mandrels. Therefore, magnets tend to exhibit quenching and detraining behaviors. Nb-Ti and Nb_3Sn accelerator magnets, except those with significant localized strand and cable degradations, quench before index loss caused joule heating becomes significant.

At 2 T, T_c of Bi-2212 is ∼35 K, where the specific heat of materials is much higher than at 4.2 K. For example, the specific heat of Cu is 390 $kJ\,m^{-3}\,K^{-1}$ at 35 K, 2 orders higher than at 4 K. The enthalpy of the Bi-2212 wire used in this study at 35 K is 5.6 MJ/m^3. Note at the quench current of 3600 A, the index loss caused by joule heating $E_q J_q$ is greater than 0.93 MW/m^3. The above semiquantitative analysis, together with the coil resistive voltage measurement, leads us to believe that our magnet likely consistently quenched at a low J_c location at the peak field region primarily due to index loss–induced joule heating of the superconductors, and to a less degree, due to ac losses of superconductors. This conclusion is consistent with the general hypothesis that the high enthalpy margin of high-temperature superconductors might lead to magnets without quench training (but currently with other issues). The low J_c region is likely caused by local leakage. This explains the quench behavior shown in Fig. 5 and the fast ramping shown in Fig. 6 for which little joule heating due to index loss is expected.

C. Field quality

Compared to other high-temperature superconducting accelerator magnet designs, a strength of the canted-cosine-theta magnet design for Bi-2212 is that good accelerator field quality is possible. Figures 7 and 8 indicate that the field error due to persistent currents is rather small. The field hysteresis is 0.4 mT at the magnet current of 2000 A (bore field = 0.912 T) at a current ramp rate of 30 A/s. In comparison, the field hysteresis for a CORC®, four-layer canted-cosine-theta magnet is ∼50 mT at a current of 2 kA (bore field = 0.946 T; peak field on the conductor = 1.06 T) [20]. For an aligned block, ROEBEL magnet, the field error due to persistent currents is on the order of 0.15%–0.20%, but field errors due to eddy current between tapes and an inductive copper quench protection ring are large, ∼17 mT (Hall probe measurement, 156 units), at a current of 2 kA (bore field = 1.09 T) at 300 A/s and Hall probe field measurement shows a strong dependence on ramp rate [15,50]. Even compared to Nb_3Sn, the field errors at low magnet currents are smaller. A 11 T cosine-theta Nb_3Sn dipole fabricated with high J_c Restacked Rod Process (RRP®) Nb_3Sn strands has a larger persistent current effect in the main dipole field at low magnet currents (the error is ∼0.8% at 2 kA, at which the main dipole field is ∼2 T (when current is ramped up) [51,52]. Field harmonics of Bi-2212 canted-cosine-theta magnets and their dynamics will be further studied with a rotating coil measurement.

D. Future development

There are several implications of this work that need to be considered in the future. The magnet described in this paper is suitable as an insert to be tested in large bore Nb_3Sn dipole magnets (e.g., a 90-mm bore, 8.2 T Nb_3Sn magnet CCT5 at LBNL [40]). This work paves the way for constructing a longer and higher field demonstration magnet using wider and higher-current cables such as the 7.8 mm wide, 17-strand cable used in RC5 and RC6 [23,31] to generate a stand-alone 5 T dipole field, a goal that has been used to motivate the development of accelerator magnets using high-temperature superconductors and measure its progress. Such magnets may be further integrated with the CCT6, a large bore (120 mm) 12 T Nb_3Sn dipole magnet [53], to build to explore the operation of Nb_3Sn/HTS hybrid magnets in the field range of 12–20 T.

The fast-ramping capability of high-temperature superconducting magnets may be of practical importance. Fast cycling superconducting magnets are used in synchrotrons of the FAIR (Facility of Antiproton and Ion Research); the main dipole magnets of SIS100 are fast ramped superferric magnets of the window frame type with a nominal field of 1.9 T at a current of 13.2 kA, a ramp rate of 4 T/s, and a continuous cycle frequency of 1 Hz [54]. The magnet coils are made of Nuclotron-type cable based on Nb-Ti wires cooled by forced flow two-phase helium. An upgrade of the LHC injection chain up to an extraction energy of 1 TeV is one of the steps considered to improve the performance of the whole LHC accelerator complex. The magnets for this upgrade require a central magnetic field from 2 to 4.5 T, and a field ramp rate ranging from 1.5 to 2.5 T/s. With ∼10% margin, the field ramp rate of ∼0.5 T/s is also feasible for Nb-Ti magnets, actively cooled by liquid Helium, and wound not lead to large quench current reduction for strands with small filament sizes and twist pitches and optimized interstrand resistances. For example, some UNK Nb-Ti magnets were tested to ramp rates up to ∼0.4 T/s with flat ramp rate dependence [55]. High-temperature superconductors have high critical transition temperatures and enthalpy margins that are orders of magnitude larger than those of Nb-Ti and Nb_3Sn. For Bi-2212 magnets to be

used as fast ramping magnets, both the eddy current losses and the hysteresis loss will need to be further reduced. A potential benefit is to work at >10 K, at which the cryogenic cooling efficiency is improved. Technical issues such as material fatigue and quench detection and protection will need further investigation.

VI. SUMMARY

We have built and operated the world's first high-temperature superconducting Bi-2212 canted-cosine-theta dipole magnet (1.64 T dipole field in 30.8 mm bore), validating the canted-cosine-theta magnet design for a promising high-field superconductor and illustrating the fabrication scheme. The magnet exhibited no quench training and no thermal cycles or quench-induced damages. Among all high-temperature superconducting magnets built thus far, this magnet is distinguished by low magnetic field errors, potentially qualifying it for accelerator magnets that demand field quality with an accuracy of about 10^{-3}. This work also identified a performance gap between wire and coil, potential causes, and solutions. The results encourage further development of high-field Bi-2212 canted-cosine-theta superconducting magnets as a tool for particle physics and other scientific disciplines.

ACKNOWLEDGMENTS

The work at Lawrence Berkeley National Laboratory (LBNL) was supported by the U.S. Department of Energy (DOE), Office of Science, Office of High Energy Physics (OHEP) through the U.S. Magnet Development Program under Contract No. DE-AC02-05CH11231. The work at NHMFL is supported by the US DOE Office of High Energy Physics under Grant No. DE-SC0010421 and by the NHMFL, which is supported by NSF under Grant No. DMR-1644779, and by the State of Florida. The wire used was developed by Dr. Yibing Huang with Bruker OST LLC and Dr. Andrew Hunt and Dr. Marvis White with the nGimat LLC (now Engi-Mat LLC); they were supported by the DOE OHEP with a Small Business Innovation Research (SBIR) award under Contract No. DE-SC0009705. We thank the support of our dedicated technical staff: Timothy Bogdanof (cryogenic operations), Andy Lin and Hugh Higley (cable fabrication and insulation), Jordan Taylor, Robert Memmo (testing), Mark Krutulis (winding and impregnation), James Swanson (impregnation), Matt Reynolds (assembly), Max Maruszewski (machining) at LBNL, and Lamar English (heat treatment) at NHMFL.

[1] A. Tollestrup and E. Todesco, The development of superconducting magnets for use in particle accelerators: From the Tevatron to the LHC, Rev. Accel. Sci. Technol. **01**, 185 (2008).

[2] K.-H. Mess, P. Schmüser, and S. Wolff, *Superconducting Accelerator Magnets* (World Scientific, Singapore, 1996).

[3] M. Anerella *et al.*, The RHIC magnet system, Nucl. Instrum. Methods Phys. Res., Sect. A **499**, 280 (2003).

[4] C. Liu, D. Bruno, A. Marusic, M. Minty, P. Thieberger, and X. Wang, Mitigation of persistent current effects in the RHIC superconducting magnets, Phys. Rev. Accel. Beams **22**, 111003 (2019).

[5] L. Rossi, Superconductivity: Its role, its success and its setbacks in the Large Hadron Collider of CERN, Supercond. Sci. Technol. **23**, 034001 (2010).

[6] L. Bottura, G. de Rijk, L. Rossi, and E. Todesco, Advanced accelerator magnets for upgrading the LHC, IEEE Trans. Appl. Supercond. **22**, 4002008 (2012).

[7] E. S. G. Collaboration, Update of the European strategy for particle physics, 2020, http://home.cern/sites/default/files/2020-06/2020%20Update%20European%20Strategy.pdf.

[8] R. Palmer, Muon colliders, Rev. Accel. Sci. Technol. **07**, 137 (2014).

[9] D. Whyte, J. Minervini, B. LaBombard, E. Marmar, L. Bromberg, and M. Greenwald, Smaller & sooner: Exploiting high magnetic fields from new superconductors for a more attractive fusion energy development path, J. Fusion Energy **35**, 41 (2016).

[10] W. D. Markiewicz *et al.*, Design of a superconducting 32 T magnet with REBCO high field coils, IEEE Trans. Appl. Supercond. **22**, 4300704 (2012).

[11] H. W. Weijers *et al.*, Progress in the development and construction of a 32-T superconducting magnet, IEEE Trans. Appl. Supercond. **26**, 4300807 (2016).

[12] P. Wikus, W. Frantz, R. Kümmerle, and P. Vonlanthen, Commercial gigahertz-class NMR magnets, Supercond. Sci. Technol. **35**, 033001 (2022).

[13] C. Völlinger, M. Aleksa, and S. Russenschuck, Calculation of persistent currents in superconducting magnets, Phys. Rev. ST Accel. Beams **3**, 122402 (2000).

[14] G. A. Kirby *et al.*, First cold powering test of REBCO Roebel wound coil for the EuCARD2 future magnet development project, IEEE Trans. Appl. Supercond. **27**, 4003307 (2017).

[15] L. Rossi and C. Senatore, HTS accelerator magnet and conductor development in Europe, Instruments **5**, 8 (2021).

[16] W. Goldacker, F. Grilli, E. Pardo, A. Kario, S. I. Schlachter, and M. Vojenčiak, Roebel cables from REBCO coated conductors: A one-century-old concept for the superconductivity of the future, Supercond. Sci. Technol. **27**, 093001 (2014).

[17] X. Wang, S. Caspi, D. R. Dietderich, W. B. Ghiorso, S. A. Gourlay, H. C. Higley, A. Lin, S. O. Prestemon, D. van der Laan, and J. D. Weiss, A viable dipole magnet concept with REBCO CORC® wires and further development needs for high-field magnet applications, Supercond. Sci. Technol. **31**, 045007 (2018).

[18] X. Wang, D. R. Dietderich, J. DiMarco, W. B. Ghiorso, S. A. Gourlay, H. C. Higley, A. Lin, S. O. Prestemon, D. van der Laan, and J. D. Weiss , A 1.2 T canted cos ϑ dipole magnet using high-temperature superconducting CORC® wires, Supercond. Sci. Technol. **32**, 075002 (2019).

[19] X. Wang, S. A. Gourlay, and S. O. Prestemon, Dipole magnets above 20 Tesla: Research needs for a path via

high-temperature superconducting REBCO conductors, Instruments **3**, 62 (2019).
[20] X. Wang *et al.*, Development and performance of a 2.9 Tesla dipole magnet using high-temperature superconducting CORC® wires, Supercond. Sci. Technol. **34**, 015012 (2021).
[21] D. C. Larbalestier *et al.*, Isotropic round-wire multifilament cuprate superconductor for generation of magnetic fields above 30 T, Nat. Mater. **13**, 375 (2014).
[22] J. Jiang *et al.*, High performance Bi-2212 round wires made with recent powders, IEEE Trans. Appl. Supercond. **29**, 6400405 (2019).
[23] T. Shen *et al.*, Stable, predictable and training-free operation of superconducting Bi-2212 Rutherford cable racetrack coils at the wire current density of 1000 A/mm^2, Sci. Rep. **9**, 10170 (2019).
[24] K. Zhang *et al.*, Tripled critical current in racetrack coils made of Bi-2212 Rutherford cables with overpressure processing and leakage control, Supercond. Sci. Technol. **31**, 105009 (2018).
[25] P. Ferracin *et al.*, Recent test results of the high field Nb_3Sn dipole magnet HD2, IEEE Trans. Appl. Supercond. **20**, 292 (2010).
[26] J. Perez *et al.*, 16 T Nb_3Sn racetrack model coil test result, IEEE Trans. Appl. Supercond. **26**, 4004906 (2016).
[27] D. R. Dietderich, T. Hasegawa, Y. Aoki, and R. M. Scanlan, Critical current variation of Rutherford cable of Bi-2212 in high magnetic fields with transverse stress, Physica (Amsterdam) **341C**, 2599 (2000).
[28] T. Shen, A. Ghosh, L. Cooley, and J. Jiang, Role of internal gases and creep of Ag in controlling the critical current density of Ag-sheathed $Bi_2Sr_2CaCu_2O_x$ wires, J. Appl. Phys. **113**, 213901 (2013).
[29] A. V. Zlobin, I. Novitski, and E. Barzi, Conceptual design of a HTS dipole insert based on Bi2212 Rutherford cable, Instruments **4**, 29 (2020).
[30] S. Caspi *et al.*, Canted–Cosine–Theta magnet (CCT)—a concept for high field accelerator magnets, IEEE Trans. Appl. Supercond. **24**, 4001804 (2014).
[31] T. Shen and L. Garcia Fajardo Superconducting accelerator magnets based on high-temperature superconducting Bi-2212 round wires, Instruments **4**, 17 (2020).
[32] P. Chen, U. P. Trociewitz, M. Dalban-Canassy, J. Jiang, E. E. Hellstrom, and D. C. Larbalestier, Performance of titanium oxide–polymer insulation in superconducting coils made of Bi-2212/Ag-alloy round wire, Supercond. Sci. Technol. **26**, 075009 (2013).
[33] J. Lu, D. McGuire, H. Kandel, Y. Xin, P. Chen, J. Jiang, U. Trociewitz, E. Hellstrom, and D. Larbalestier, Ceramic insulation of $Bi_2Sr_2CaCu_2O_{8-x}$ round wire for high-field magnet applications, IEEE Trans. Appl. Supercond. **26**, 7701005 (2016).
[34] H. Kandel, J. Lu, J. Jiang, P. Chen, M. Matras, N. Craig, U. Trociewitz, E. Hellstrom, and D. Larbalestier, Development of TiO_2 electrical insulation coating on Ag-alloy sheathed $Bi_2Sr_2CaCu_2O_{8-x}$ round-wire, Supercond. Sci. Technol. **28**, 035010 (2015).
[35] I. Hossain, J. Jiang, M. Matras, U. Trociewitz, J. Lu, F. Kametani, D. Larbalestier, and E. Hellstrom, Effect of sheath material and reaction overpressure on Ag protrusions into the TiO_2 insulation coating of Bi-2212 round wire, IOP Conf. Ser. **279**, 012021 (2017).
[36] T. Shen, J. Jiang, F. Kametani, U. P. Trociewitz, D. C. Larbalestier, and E. E. Hellstrom, Heat treatment control of Ag-$Bi_2Sr_2CaCu_2O_x$ multifilamentary round wire: Investigation of time in the melt, Supercond. Sci. Technol. **24**, 115009 (2011).
[37] T. Shen, P. Li, and L. Ye, Heat treatment control of Bi-2212 coils: I. Unravelling the complex dependence of the critical current density of Bi-2212 wires on heat treatment, Cryogenics **89**, 95 (2018).
[38] G. Ambrosio, Nb_3Sn high field magnets for the high luminosity LHC upgrade project, IEEE Trans. Appl. Supercond. **25**, 4002107 (2014).
[39] S. Yin, D. Arbelaez, J. Swanson, and T. Shen, Epoxy resins for vacuum impregnating superconducting magnets: A review and tests of key properties, IEEE Trans. Appl. Supercond. **29**, 7800205 (2019).
[40] D. Arbelaez *et al.*, Status of the Nb_3Sn canted-cosine-theta dipole magnet program at Lawrence Berkeley National Laboratory, IEEE Trans. Appl. Supercond. **32**, 4003207 (2021).
[41] J. L. Rudeiros Fern'andez *et al.*, Assembly and mechanical analysis of the canted-cosine-theta subscale magnets, IEEE Trans. Appl. Supercond. **32**, 4006505 (2021).
[42] Y. Oz, D. Davis, J. Jiang, E. E. Hellstrom, and D. C. Larbalestier, Influence of twist pitch on hysteretic losses and transport J_c in overpressure processed high J_c Bi-2212 round wires, Supercond. Sci. Technol. **35**, 064004 (2022).
[43] J. Rochester, C. Myers, M. Sumption, T. Shen, M. Majoros, and E. Collings, The magnetization of Bi: 2212 Rutherford cables for particle accelerator applications, IEEE Trans. Appl. Supercond. **31**, 6440305 (2021).
[44] L. Garcia Fajardo *et al.*, First demonstration of high current canted-cosine-theta coils with Bi-2212 Rutherford cables, Supercond. Sci. Technol. **34**, 024001 (2021).
[45] D. Wesolowski, M. Rikel, J. Jiang, S. Arsac, and E. Hellstrom, Reactions between oxides and Ag-sheathed $Bi_2Sr_2CaCu_2O_x$ conductors, Supercond. Sci. Technol. **18**, 934 (2005).
[46] M. Dalban-Canassy, D. Myers, U. Trociewitz, J. Jiang, E. Hellstrom, Y. Viouchkov, and D. Larbalestier, A study of the local variation of the critical current in Ag-alloy clad, round wire $Bi_2Sr_2CaCu_2O_{8+x}$ multi-layer solenoids, Supercond. Sci. Technol. **25**, 115015 (2012).
[47] T. Shen, J. Jiang, F. Kametani, U. Trociewitz, D. Larbalestier, J. Schwartz, and E. Hellstrom, Filament to filament bridging and its influence on developing high critical current density in multifilamentary $Bi_2Sr_2CaCu_2O_x$ round wires, Supercond. Sci. Technol. **23**, 025009 (2010).
[48] P. Li, L. Ye, J. Jiang, and T. Shen, RRR and thermal conductivity of Ag and Ag-0.2 wt.% Mg alloy in Ag/Bi-2212 wires, IOP Conf. Ser. **102**, 012027 (2015).
[49] M. Matras, J. Jiang, U. Trociewitz, D. Larbalestier, and E. Hellstrom, Process to densify $Bi_2Sr_2CaCu_2O_X$ round wire

with overpressure before coil winding and final overpressure heat treatment, Supercond. Sci. Technol. **33**, 025010 (2020).

[50] C. Petrone, H. Bajas, L. Bottura, G. Kirby, L. Rossi, and S. Russenschuck, Measurement and analysis of the dynamic effects in an HTS dipole magnet, IEEE Trans. Appl. Supercond. **28**, 4604404 (2018).

[51] X. Wang *et al.*, Validation of finite-element models of persistent-current effects in Nb_3Sn accelerator magnets, IEEE Trans. Appl. Supercond. **25**, 4003006 (2015).

[52] G. Chlachidze *et al.*, Field quality study of a 1-m-long single-aperture 11-T Nb_3Sn dipole model for LHC upgrades, IEEE Trans. Appl. Supercond. **24**, 4000905 (2013).

[53] L. Brouwer, M. Juchno, D. Arbelaez, P. Ferracin, and G. Vallone, Design of CCT6: A large aperture, Nb_3Sn dipole magnet for HTS insert testing, IEEE Trans. Appl. Supercond. **32**, 4001805 (2022).

[54] E. Fischer, H. G. Khodzhibagiyan, and A. D. Kovalenko, Full size model magnets for the FAIR SIS100 synchrotron, IEEE Trans. Appl. Supercond. **18**, 260 (2008).

[55] A. Zlobin, UNK superconducting magnets development, Nucl. Instrum. Methods Phys. Res., Sect. A **333**, 196 (1993).